On the Estimation of Snow Thickness Distributions over Sea Ice Using the Thermal Dependence of Backscatter

David G. Barber[1] and Son V. Nghiem[2]

Journal of Geophysical Research (Oceans)

[1]Centre for Earth Observation Science, Department of Geography,
University of Manitoba, Winnipeg, Manitoba, Canada, R3T 2N1,

[2]Center for Space Microelectronics Technology
Jet Propulsion Laboratory, MS 300-235
California Institute of Technology
4800 Oak Grove Drive
Pasadena, CA 91109

Abstract

Our understanding of snow distributions in the polar regions is severely restricted due to the heterogeneity, both in space and time, of this solid precipitate. Processes such as vapour and mass fluxes across the interface are, to a large extent, controlled by the presence and geophysical state of the snow cover on sea ice. Numerous studies have shown the importance of snow cover in ecosystem processes and particularly in photosynthtically active radiation (PAR) extinction. Researchers are currently exploiting developments in electromagnetic interaction theory in an attempt to measure snow thickness distributions remotely. In this paper, we investigate the dependence of radar backscatter on snow thickness over smoth first-year sea ice. We use data from the Seasonal Sea Ice Monitoring and Modelling Site (SIMMS) located in the Canadian Archipelago.

Results show that the thermodynamics of the snow cover affect wave propagation, attenuation, and scattering through the control that brine distributions exert on interfacial characteristics of the snow and ice layers. The effect is specific to certain ranges of salinity, surface roughness, and thickness of sea ice. We describe the phenomenon responsible for this effect using a microwave model consistently for both complex effective permittivities and backscattering coefficients coupled to a one-dimensional thermodynamic model. We validate the physical principles using in situ field data. We then discuss the potential of synthetic aperature radar (SAR) in estimating snow thickness distributions under these specific conditions using both observed (ERS-1) and modelled microwave scattering.

1. Introduction

The snow cover on sea ice is an important physical variable which impacts energy, geophysical and chemical processes operating across the ocean-sea ice-atmosphere (OSA) interface. Although this system is highly coupled, it is illustrative to consider some specific relationships between the snow cover on sea ice and physical and biological processes operating across this interface.

Physically, the snow cover contributes to determining the magnitude and rate of ice growth and decay [*Maykut*, 1978]. The partitioning of components of the sea ice energy balance is intimately linked with the thermal diffusivity of the snow cover and the absorption, reflection, and transmission of climatological shortwave radiation [*Grenfell and Maykut*, 1977]. Physical properties of the snow-sea ice volume affect conductive, turbulent and radiative energy exchanges between the underlying hydrosphere and overlying atmosphere. The spatial and temporal variations in these exchanges have an impact on virtually all of the physical processes operating across the OSA interface over a range of scales from local to hemispheric.

Biologically, snow and sea ice are integral components of specific species ecotones. On sea ice, the epontic (sub-ice) primary production is known to be light limited [*Welch and Bergmann*, 1989]. Due to the exponential nature of the absorption properties of Photosynthetically Active Radiation (PAR; 0.4 to 0.7 μm) most of the attenuation of PAR frequencies occurs within the snow volume. The epontic communities have evolved to thrive within a range of snow cover conditions; too much snow cover starves the organism of light and too little snow over stimulates the organism thereby lowering the total production [*Cota and Horne*, 1989]. Higher levels of the trophic system, particularly ringed seals (*Phoca hispida*), have evolved within a niche whereby they utilize the snow cover on sea ice for protection from predation and the harsh environment of the Arctic winter [*Smith and Stirling*, 1977].

From the perspective of climate variability and change, a consistent representation in general circulation models is that the polar regions of the planet should experience an amplification in temperature under various scenarios of a CO_2 enhanced atmosphere. This amplification is due to a

variety of feedback mechanisms operating between the atmosphere and the surface. Although a variety of these feedbacks have been identified the 'sea ice-albedo' feedback mechanism appears to be a significant component of this system [*Barry et al.*, 1993]. Under warmer atmospheric conditions we can expect an increase in precipitation. We are, however, uncertain of the first-order response of the system to this increase in precipitation, either: 1) the sea ice will ablate earlier in the marginal regions because a thicker snow cover will minimize the equilibrium thickness of the sea ice, or; 2) an increase in precipitation will cause a delay in the seasonal ablation of the sea ice due to an increase in the shortwave albedo, during the critical spring ablation period. To gain an understanding of these processes we require information on the snow thickness distributions over sea ice.

2. Background and Objectives

Over the past 8 years (1990 to 1997), a team has been conducting in situ process studies on sea ice near Resolute Bay, Northwest Territories, Canada. During various experiments, it became evident that the microwave scattering coefficient (σ°) at 5.3 GHz was affected by environmental conditions such as cloud cover, temperature, and precipitation. Detailed surface validation data were used to investigate the relationship between physical, electrical, and energy balance characteristics of the seasonal evolution of σ° for both 1992 [*Barber et al.*, 1994b] and 1993 [*Barber et al.*, 1996]. These statistical studies indicated that a relationship existed between the time series σ° and physical aspects which control the temperature regime through the snow-sea ice interface. In both years we attributed the changes in the microwave response to a change in the geophysical characteristics of the snow and ice surface which was in turn created by changes in the surface energy balance of the ocean-sea ice-atmosphere system.

A more focused study was then conducted to examine the relationship between sea ice thermodynamics and microwave scattering within the spring transitional season. In this work, we examined the role of cloud cover in changing the microwave scattering over sea ice when atmospheric temperatures were less than -10°C (i.e., no water in liquid phase within the

snow cover). Results showed that a cloud cover caused an increase in scattering over low-magnitude scattering targets (i.e., smooth first-year sea ice) by several dB [*Barber and Thomas*, 1998] but that this change in scattering was not evident in scattering targets above about -19 dB (i.e., rough first-year, rubble or multiyear sea ice). We concluded that the observed phenomenon was related to the effect of temperature changes on the brine volume within the basal layer of the snow cover and/or within the frazil matrix near the upper interface of first-year sea ice. We also suggested that the relationship may be related to snow thickness distributions because of the heat capacity of snow relative to that of sea ice and the associated thermodynamic control on brine volume and complex permittivity [*Barber and Thomas*, 1998].

In this work, we extend our previous results and examine the physical mechanisms which cause this subtle change in scattering. We conceptualize this problem as a 'geophysical-thermodynamic-scattering' relationship. We are interested in how the thermodynamics affect the geophysics of the system (including dielectrics) and how this change is manifested in scattering at microwave frequencies. In particular, we are interested in the relative contributions of the basal snow layer and the interfacial frazil ice layer to the observed change in scattering. From a physical perspective, this can be attributed to the following potential mechanisms: 1) scattering from large kinetic growth grains in the snow basal layer itself, 2) scattering from brine inclusions within the snow basal layer, 3) scattering from brine pockets within the surface frazil layer of the first-year sea ice, and 4) scattering from small scale roughness at the interface between snow and sea ice. The second and third mechanisms are thermodynamically driven through the effect of temperature changes on brine volume (particularly once basal layer snow temperatures exceed about -7°C). Rough surface scattering depends on permittivities of snow and sea ice, which is relate to the temperature dependence of the brine liquid phase distributions. Temperature metamorphism also controls grain size but in a much more complex fashion. In each case, snow thickness distributions are related to these mechanisms by means of the thermodynamics which determine the temperature profile through the snow and sea ice. In this paper, we examine these issues from both modelling and observational perspectives.

3. Methods

Data for this research were collected during the Seasonal Sea Ice Monitoring and Modelling Site experiment in 1993 (SIMMS'93). SIMMS is a multidisciplinary research program which has been conducted annually from Resolute Bay on Cornwallis Island in the central portion of the Canadian Arctic Archipelago (Figure 1). This longitudinal field study was initiated to collect baseline geophysical data from snow covered sea ice, to relate these to climatic and biological processes operating through the ocean-ice-atmosphere interface, and to develop an understanding of how remote sensing data can be used to parameterize selected variables [*LeDrew and Barber*, 1994]. The methods pertinent to the objectives of this paper are reviewed here, further details are available elsewhere [*Barber et al.*, 1994a, *Barber et al.*, 1996, *Barber and Thomas*, 1998].

3.1. Surface Measurements

Detailed physical, electrical, and energy balance variables were measured at a multiyear (MYI) site and a first-year (FYI) sea ice site over the period from 22 April to 20 June, 1993. Energy balance towers were stationed over both MYI and FYI sites. Compents of the energy balance were recorded as 15 minute averages by Campbell Scientific Instruments data loggers (model 21X). Snow and ice temperatures were measured using thermocouple profiling sensors imbedded within the snow and ice volumes.

Physical properties of the snow volume were obtained from pits located within an area immediately adjacent to a thermocouple array associated with the microclimate stations at the MYI and FYI sites. Crystal pits consisted of a small rectangular excavation of approximately 0.5 m^2 . All measurements were obtained from the diffusely illuminated snow wall perpendicular to the direct beam illumination. Snow grain photographs were obtained from each level by removing the sample with a purpose built grid and photographing them at a fixed distance using a 35 mm camera and 60 mm micro lens. These photographs were then digitized into a microcomputer where an operator identified individual snow grains. The 2-dimensional representation of the snow grain area was automatically

computed and output to a database. Snow density was measured using a gravimetric approach and salinity was measured using an Atago optical Salinometer. Further details on these methods are available elsewhere [*Barber et al.*, 1994a].

Physical properties of the sea ice volume were acquired from ice cores. The salinity, density, and temperature were measured *in situ* from the extracted cores (and continuously at the climate stations). Vertical and horizontal thin sections were prepared from the cores and photographed under polarized light to reveal details of ice microstructure. Digital analysis of the thin sections was used to derive the fractional volumes, size and shape of the inhomogeneities over the vertical dimension of the ice core. Thin sections were prepared according to a double-microtoming technique [*Shokr and Sinha*, 1994].

The segmentation of the study area into 4 consolidation periods was done using archived ERS-1 data from the accretion period, Canadian Ice Services Ice Charts, and in situ observations of snow and ice thickness as part of a reconnaissance field sampling program between April and June in 1993.

3.2 ERS-1 Data

The Earth Resources Satellite-1 (ERS-1) synthetic aperture radar (SAR) data were used in these analyses. ERS-1 is in a sun-synchronous, near polar orbit with a mean altitude of 785 km. The sensor transmits and receives vertically polarized (VV) microwavelength energy at a center frequency of 5.3 GHz (C-band). The SAR looks to the right of the spacecraft at a 23° average incidence angle and images a continuous surface swath of 100 km when it is within range of a suitably equipped ground receiving station. Processing of the ERS-1 SAR data were done at the Alaska SAR facility (ASF), University of Fairbanks, Alaska. The low resolution ASF product (4 look; 100m pixel spacing) was used here. Calibration of the image data to a microwave scattering coefficient (σ°) was done according to Olmsted [1993].

From the complete SIMMS'93 dataset we selected two cases for detailed study: May 6 with 0/10 cloud cover and a daily average air

temperature of -18°C; May 9 with 10/10 stratus cloud cover and air temperature of -11°C. We acquired 2 ERS-1 scenes from the Alaska SAR facility, local overpass times of 22:23 and 22:29 hrs (CDST) for May 6 and May 9 respectively. A program was written to compute a bivariate histogram which shows the frequency of co-occurence of $\sigma°$'s between the May 6 and May 9 dates. A nearest neighbor decision was imposed to minimize changes in radiometry due to the georectification. No change in scattering between the two dates would result in most of the histogram values occurring along the zero difference diagonal. A 1.5 dB envelope was constructed along the diagonal to illustrate significant departures in scattering between the cold and warm cases.

3.3. Microwave Modelling

The microwave scattering model implemented here includes the scattering processes from ice grains and brine inclusions in snow, brine pockets in frazil sea ice, and a small scale roughness (undeformed sea ice) at the interface between the snow and sea ice layers. This complete structure of the model allows the examination of all the scattering mechanisms set forth in the above section. Furthermore, effects on wave speed and wave attenuation in the presence of multiple species of scatterers are accounted for consistently under the strong permittivity fluctuation theory with the same statistical description used in the scattering calculations with the layered system.

The effective permittivity of an inhomogeneous medium characterizes wave speed and wave attenuation. The strong permittivity fluctuation theory [*Tsang et al.*, 1981, *Nghiem et al.*, 1996] includes the scattering effects on wave propagation due to the inhomogeneities such as ice grains and brine inclusions in snow and brine pockets in sea ice. Physically, electromagnetic waves lose energy along the propagation direction because the inhomogeneities scatter part of the wave in other directions causing the scattering loss in addition to the absorption loss. The scatterers also modify the wave speed. Thus, snow and sea ice are inherently dispersive because of the presence of the scatterers. These effects are represented by a scattering term together with the quasistatic part in the effective permittivity ε_{eff} in [1].

$$\varepsilon_{eff} = \varepsilon_{g} + \varepsilon_{sc}. \qquad [1]$$

where ε_g is the quasistatic effective permittivity determined by the Polder-van Santen mixing and ε_{sc} accounts for multiple scattering effects of the scatterers. The snow layer consists of ice grains and brine inclusions with different sizes, shapes, orientations, and permittivities of the individual constituents. In the frazil ice layer, brine pockets are non-spherical and randomly oriented because of the unaligned nature of the crystallographic c-axes of the polycrystalline ice (I_h) in this layer. Furthermore, effective permittivities of both snow and sea ice are dependent on temperature not only because the constituent permittivities are functions of temperature but also because the phase (solid ice, liquid brine, and air) distribution are driven thermodynamically [*Cox and Weeks*, 1983]. Complex expressions of effective permittivities in [1], including all of the above properties of snow and sea ice, have been derived and reported elsewhere [*Nghiem et al.*,1993, 1995a, 1996].

Backscatter from the mutiple species of scatterers is obtained under the wave theory for the snow covered sea ice. Dyadic Green's functions for layered media are used to acount for multiple reflections, refractions, and transmissions at the interfaces between air and snow, snow and sea ice, and sea ice and sea water. Effective permittivities of snow and sea ice given by [1] are used in the distorted Born approach for the scattering effects of wave propagation in inhomogeneous scattering media. In this approach, the competitive effects of wave scattering and wave loss can be visualized as follows: more scatterers give rise to stronger backscatter but scatterers deeper in the medium are partially shielded because the upper inhomogeneities scatter away some of the wave energy. The model consistently treats the backscatter and effective permittivity using the same statistical descriptions for the multiple scatterers in the layered configuration (snow covering sea ice over sea water). In this case, the ensemble average of the scattered field correlation is expressed in [2].

$$\left\langle \overline{E_s}(r)\cdot\overline{E_s^*}(r)\right\rangle = \sum_{n=1}^{2}\sum_{t=1}^{N_n}\sum_{i,j,k,l,m}^{x,y,z} k_0^4 \int_0^{2\pi} d\gamma \int_0^{\pi} d\beta \int_0^{2\pi} d\alpha$$
$$\cdot \int_{V_n} \overline{dr_n} \int_{V_n} \overline{dr_n^0}\, p_n(\alpha,\beta,\gamma) C_{t\xi niklm}\left(\overline{r_n, r_n^0};\alpha\right)$$
$$\cdot \left[\left\langle G_{0nii}\left(\overline{r,r_n}\right)\right\rangle \left\langle F_{nk}\left(\overline{r_n}\right)\right\rangle\right] \left[\left\langle G_{0nil}\left(\overline{r,r_n}\right)\right\rangle \left\langle F_{nm}\left(\overline{r_n^0}\right)\right\rangle\right]^* \qquad [2]$$

where $\overline{E}_s$ is the scattered field, $n=1$ denotes the snow layer and $n=2$ for the sea ice layer, t represents different species of scatterers, N_n is the number of species in layer n, and V_n is the volume occupied by layer n. The probability density function $p_n(\alpha,\beta,\gamma)$ is for the orientation distribution of the scatterers with Eulerian angles α, β, and γ. In [2], G is the mean dyadic Green's function, F is related to the radar transmitted waves, C is the correlation function statistically characterizing the geometrical and physical properties of the scatterers. From the scattered field correlation [2], the radar backscatter is determined by [3]

$$\sigma_{\mu\tau\nu\kappa} = \lim_{\substack{r\to\infty \\ A\to\infty}} \frac{4\pi r^2 \left\langle E_{\mu s} E_{\nu s}^*\right\rangle}{A \quad E_{ri} E_{ki}^*} \qquad [3]$$

where A is the area of the radar resolution, r is the distance between the radar and the targeted area, and E_i is the transmitted field. Wave polarizations are described with μ, ν, τ, and κ, which can be horizontal (h) or vertical (v). For the case of ERS-1 SAR, all transmitted and received polarizations are vertical ($\mu=\nu=\tau=\kappa=v$) and the backscatter is denoted with $\sigma^0 = \sigma_{\mu\tau\nu\kappa}$. Mathematical expressions for σ^0 have been derived by Nghiem et al. [1995b and references therein] for snow covered sea ice.

Furthermore, field observations indicate that there is a small scale roughness at the interface between snow and sea ice (Barber et al. 1994a). The roughness introduces discontinuities which modify the boundary condition giving rise to the rough surface scattering. In the layered system of snow cover on sea ice, the incident wave field at this interface undergoes the reflection, refraction, and transmission effects at medium boundaries and the current induced by the incident wave field on the snow-sea ice interface re-radiates and thus contributes to the total scattered field measured by the radar. The rough surface scattering depends on the

roughness characterized with the standard deviation height (σ) and the surface correlation length (L). Expressions under the Kirchhoff approximation for rough surface scattering from the layered system of snow-covered sea ice with relatively smooth surface of undeformed first-year sea ice have been derived by Nghiem et al. [1995b]. The microwave model discussed in this section will be applied to investigate the scattering mechanisms from the snow cover on sea ice undergoing thermodynamic variations at the SIMMS site using *in situ* snow, ice, and environmental parameters.

3.4. Thermodynamic Modelling

A common physically based thermodynamic model [*Maykut*, 1978, *Cox and Weeks*, 1988, and *Nakawo and Sinha*, 1981] is used to compute snow and ice temperature profiles using density and fractional volumes within both the snow and sea ice volumes. Nakawo and Sinha [1981] found that the model provided a good fit to both snow and sea ice temperature distribution data collected in the Canadian Arctic in April and February. Validation of the model within the SIMMS site and experimental conditions described here also showed excellent agreement between measured and modelled temperature profiles [*Barber*, 1992]. The model assumes constant thermal conductivities within a snow and sea ice volume. The snow/ice interface temperature (Ts/i) is computed as [4]

$$T_{s/i} = \frac{k_i h_s T_m + k_s h_i T_a}{k_s h_i + k_i h_s} \qquad [4]$$

where the temperature gradient within the snow volume (G_s) and in the sea ice (G_i) are computed by [5 and 6]

$$G_s = \frac{T_m - T_a}{(k_s/k_i)\, h_i + h_s} \qquad [5]$$

$$G_i = \frac{T_m - T_a}{h_i + (k_i/k_s)\, h_s} \qquad [6]$$

where k_S and k_i are the thermal conductivities of snow and sea ice; T_m, T_a, and $T_{S/i}$ are the temperatures of the melting point of sea ice (-1.8 °C), air temperature, and the snow/ice interface temperature, respectively; h_i and h_S are the thickness of the sea ice and snow.

An expression for computation of the effective thermal conductivity [7] of snow, was developed from data presented by Pitman and Zuckerman [1967]

$$Y = 0.282 - 1.83x + 4.545x^2 \qquad [7]$$

where x is snow density, expressed in $gm \cdot cm^{-3}$ and Y is thermal conductivity in $W \cdot m^{-1} \cdot °C^{-1}$. The expression is considered valid over the density range 0.1 $gm \cdot cm^{-3}$ to 0.6 $gm \cdot cm^{-3}$ at an average bulk snow temperature of -5°C. For bulk snow temperatures lower than -5°C an approximate solution is to subtract 0.0036 $W \cdot m^{-1} \cdot °C^{-1}$ from the value obtained from [7] for temperatures down to -27°C.

In what follows, we present observed values for physical, electrical and temperature data from the FYI site during SIMMS'93. We review the basic processes affecting the 'geophysical-thermodynamic-scattering' relationship being examine here. We then determine the physical parameters required by the microwave model from measured field data and from published empirical relationships for temperature dependent variables. Once the parameters are obtained, they are used directly in the microwave model and no parameter 'twiddling' is allowed. The calculated results are compared to determine the backscatter response to the temperature change as predicted by the model. We then examine each of the scattering components to investigate the scattering mechanisms and study how they are related to the thermodynamic variation. We then use the thermodynamic model to obtain the temperature profile in snow and sea ice for a thick snow cover with both cold and warm air temperature cases with the appropriate changes in temperature dependent parameters given by the empirical

relations. This analysis will reveal the dependence of backscatter change driven by the temperature variations as a function of the thickness of the snow cover.

4. Results and Discussion

4.1. *In Situ* Physical Properties

The snow cover at the FYI site was a typical multilayer system. The bulk salinity increased from the frazil ice surface (13 ppt) upwards into the snow layer (14-22 ppt at the 2 cm level; Figure 2). This increase in bulk salinity results from brine wicking mechanisms between the snow and ice surface and as a result of the destruction of early season frost flower formation on the ice surface. The gradual decline in salinity upwards into the snow volume results from the reduction in capillary suction at greater distances from the source (i.e., ice surface). Note that at this time in the seasonal evolution there is no systematic gravity drainage of bulk salinity within the snow cover and there is no water in liquid phase within the snow volume. The brine volumes illustrate the interaction of temperature and bulk salinity. The lower 4 cm of the snow volume contains significant amounts of brine (Figure 2) with the 2 cm layer being marginally higher than the 4 cm level due to the lower snow density (yet higher bulk salinity) at the 2 cm level. We expect snow metamorphism to be dominated by temperature gradient processes. The grains in the centre of the snow volume will be growing by about 0.1 to 0.5 $mm^2 \cdot d^{-1}$ [*Barber et al.*, 1994a]. With smaller grains being integrated into larger grains due to different surface pressures [*Colbeck*, 1982]. Grains in the basal layer will grow by vapour diffusion under these temperature conditions and take on a kinetic growth form typical of 'depth hoar' [*Colbeck*, 1986]. The complex permittivity of the snow volume and ice surface (Figure 2) is dominated by the brine volume of the material and forms a fundamental 'geophysical-thermodynamic' link being examined here.

4.2. Modelling Evidence

4.2.1. Physical Parameters

Field data show that the total snow layer (all 12-cm) consists of dry snow (i.e., no water in liquid phase) with very small rounded ice grains in the top 8 cm; large kinetic growth grains with significant salinity and brine volume in the basal layer of the snow cover (2 and 4 cm levels). Since the dry snow is transparent to electromagnetic waves at 5.3 GHz and the scattering is estimated to contribute only a small fraction of a dB to the total scattering due to the small size of ice grains, the dry snow layer will be ignored in the following analysis. Profiles of physical parameters used in modelling the thin snow case (Figure 3) are derived from the field data and from published empirical relations for temperature dependent variables.

For the case of the cold snow cover over sea ice, the bulk (averaged) physical paremeters are listed in Table 1. The fractional volumes of ice, brine, and air are determined by the thermodynamic distribution of the phases based on observed temperature and salinity [*Cox and Weeks*, 1983]. The permittivity of ice depends on temperature and its real part is obtained from an empirical relation by Vant et al. [1978] and the imaginary part from Tiuri et al. [1984]. The complex permittivity of brine is also a function of temperature as given by Stogryn and Desargant [1985]. The empirical relations are also applied to the sea ice layer (at a different temperature according to the in situ temperature profile).

Note that the parameters are obtained from the input data reported in the previous section, measured above the depth of 20 cm, in the 1.7-m thick first year sea ice for all cases. This will not affect the conclusion of this study since the waves at C band (5.3 GHz) cannot penetrate much below the depth of 20 cm in the lossy sea ice. Sea water has a salinity of 30 ppt at the melting temperature of -1.8 deg C for saline water, which are used to obtain sea water permittivity given by Klein and Swift [1977]; however, this parameter is not important because the FYI is thick. Similarly, the parameters for the warm snow case are shown in Table 2.

Scatterer sizes and shapes are modelled with volumetric correlation lengths which are related to physical sizes by the equicorrelation volume method [*Yueh et al.*, 1990, *Nghiem et al.*, 1996]. For ice grains in the cold

basal snow layer, the average minor and major axes are 2.8 and 4.3 mm, respectively; these correpond to correlation lengths of 0.8 and 1.2 mm by a factor of $1/(2\cdot\sqrt[3]{6})$ [*Yueh et al.*, 1990, *Nghiem et al.*, 1996]. In the measurements of snow grain size, grains were transferred from the snow sample and laid on a flat surface to be photographed. Since the minor and major axes are different, we assume that, on average, the ice grains have a prolate spheroidal shape with the given axes so that they lie on the specimen surface in a stable position and appear as elliptical cross section with the same axes as in the photograph [*Barber et al.*, 1994a]. Within the basal snow layer, we use a random distribution for the ice grain orientation.

Data on brine inclusion size and shape in snow are not available directly from in situ measurements. We assume that the inclusions have a spherical shape with an average size similar to the average of the ice grain axes given above; this results in a correlation length of (0.8+1.2)/2=1 mm for the brine inclusions. This is because the snow is in the pendular regime and the brine inclusions are unconnected and distributed in the intercellular space between randomly oriented ice grains. Note that the liquid brine data in Table 1 is well below the liquid saturation transition into the snow funicular regime [*Colbeck*, 1982].

In sea ice, brine is sandwiched between ice platelet boundaries and forms brine pockets, which are substantially nonspherical. The average measured major axis of the brine pockets is 1.6 mm for the frazil ice layer [*Shokr*, 1997] corresponding to an approximate correlation length of 0.5 mm. For a substantially nonspherical shape of the sandwiched brine, we take the brine pockets to be randomly oriented oblate spheroids with a minor correlation length in the submillimeter scale of 0.1 mm. The random orientation is observed for brine pockets in the frazil ice [*Shokr*, 1997]. Such random orientation is common in frazil ice within the SIMMS study area, due to the unalignment of c-axes in the frazil polycrystalline ice structure [*Shokr and Sinha*, 1994].

When the temperature increases, the brine volumes in snow and sea ice also increase to stay on the eutectic phase distribution curve [*Cox and Weeks*, 1983]. The higher temperature in the warm case, of snow covered sea ice, causes a melting effect at the adjacent ice grain boundary, thereby increase brine volume at the expense of ice volume in both snow and sea ice [*Barber et al.*, 1994a]. We use this effect to estimate the scatterer correlation

lengths with the same axial ratios for the warm case by means of the conservation of scatterer numbers [*Nghiem et al.*, 1997]. In this case, the linear size increases by the cubic root of the volume expansion ratio. The results for the brine correlation length in snow is 1.3 mm and for those in sea ice are 0.67 mm and 0.14 mm. Data on minor and major axes of ice grains in snow do not show differences within the measurement uncertainty and are taken to be unchanged between the warm and cold cases. For the undeformed smooth FY sea ice in both the cold and warm cases, the average roughness parameters at the interface between snow and sea ice is estimated to be 0.6 cm for the standard deviation height and 15 cm for the surface correlation length. These roughness parameters are based on replicate sampling with a photographic surface roughness instrument [*Clausi and Zagon*, 1993].

4.2.2. Backscatter Response to Temperature Change

Input parameters required for the microwave model are 1) fractional volumes, 2) correlation lengths, and 3) and permittivities of the different species of scatterers in the snow and sea ice layers within given thicknesses. These parameters are taken from Tables 1 and 2 to calculate both effective permittivities and backscattering coefficients. Furthermore, the roughness parameters are used to obtain the surface scattering contribution, subject to the scattering loss characterized by the effective permittivities and to the layer effects of snow covered sea ice.

For the cold snow cover case, the vertical backscatter is -22.1 dB at the opreating frequency of 5.3 GHz and at the ERS-1 look angle of 23 deg. In the warm snow cover case, the vertical backscatter at the same frequency and the same incidence angle increases to -18.6 dB. Thus, the model estimates an increase of 3.5 dB associated with the physical changes induced by the temperature increase in the snow cover on smooth undeformed FY sea ice. The results show a slight increase in the effective permittivity of the basal snow and a stronger increase in the effective permittivity of fazil ice.

The backscatter increase is contributed by several factors: 1) the increase in brine permittivities with temperature in both snow and sea ice

which enhances the contrast between brine and the background medium and thus strengthens the scattering effects, 2) the higher brine volumes in snow and sea ice at the higher temperature, 3) the enlargement of brine scatterers which leads to larger cross sections and stronger backscatter, and 4) the increase in effective permittivity contrast across the interface between snow and sea ice. The results for effective permittivities and backscatter response to the temperature change are summarized in Table 3.

4.2.3. Scattering Mechanisms in Snow Covered Sea Ice

To investigate the contributions from different scattering mechanisms in the snow covered sea ice system, we take out the scattering effects of each individual component and calculate the change in the total backscatter. To remove the scattering effects of ice grains in snow, we reduce the grain size to zero. This approach consistently accounts for the reduction in backscattering as well as the scattering loss while preserving the salinity and the quasistatic effective permittivity of snow. In this case, the effective permittivity in [1] becomes $\varepsilon_{eff} = \varepsilon_g$. The same approach is applied to brine in snow and sea ice. The rough surface scattering is removed by setting the standard deviation height to zero. The reduction in backscatter between these cases, from that of the case with all scattering mechanisms included, are presented in Figure 4 for both the cold and warm snow covered sea ice. This analysis approach will result in a large backscatter reduction when an important scattering mechanism is eliminated.

Figure 4 shows that the scattering from the basal snow layer is most important in both cold and warm cases. The brine inclusions in sea ice have some contribution to the total scattering and the contribution from the surface scattering of the smooth FY ice contributes the least to the scattering change. In the cold case, removing the ice grain scattering in the basal snow reduces the backscatter by 3.6 dB. This indicates that the grain scattering accounts for a little more than half of the total scattering. The other half of the total backscatter is primarily from the brine in snow and sea ice. As the temperature increases in the warm case, this situation is reversed and the brine scattering becomes larger than that of ice grains. These results indicate that the increase in the backscatter between the cold and warm

snow cases is caused by the thermal modification on brine volumes in snow and sea ice.

To confirm this result, we use the model to simulate the desalination effects which results in a weaker increase in backscatter since the total brine volume is decreased by the desalination. This explains the observation that the backscatter increase with temperature does not occur for MY sea ice as observed by Barber and Thomas (1998), which contains much less salinity compared to that of FY ice.

In all of the above cases for smooth FY ice, the roughness is small and its effects driven by the temperature change are not obvious. We amplify the roughness effects by using the model to simulate the results for rougher surfaces, but still smooth enough to satisfy the validity condition of the Kirchhoff approximation. The simulation shows an increase in backscatter between the cold and warm cases $\sigma^0_{warm} - \sigma^0_{cold} > 0$ having a rougher surface (the same roughness is used in both cases). This is because the permittivity contrast between snow and sea ice across the interface increases with higher temperature as shown in Tables 1 and 2. However, simulations with several pairs of cold and warm cases at different roughnesses show that the amount of backscatter increase is weakened as the surface becomes rougher ($\Delta\sigma^0 = \sigma^0_{warm=} - \sigma^0_{cold}$ is smaller with larger roughness). This trend follows ERS-1 observations reported elsewhere [*Barber and Thomas*, 1998].

4.2.4. Thermodynamic Effects with Different Snow Thickness

To study the dependence of snow thickness on the change in microwave scattering we consider a 24 cm thick snow cover (double the snow thickness examined above). Thermodynamically, this thicker snow cover results in a smaller temperature gradient within the snow volume and an elevated temperature (relative to the thin snow case) at the snow/ice interface. Associated changes in physical parameters occur because of the relationship between the geophysics and thermodynamics of the volume. For example, the thick cold snow cover warms the surface temperature between the snow and sea ice to -10.2 ° C compared to -12.9 ° C for the thin cold snow case. Consequently, the brine volumes in the basal snow and the

frazil ice above and below the interface increase. The physical parameters are plotted in Figure 5. All permittivities are changed as functions of temperature and the scattering is modified by such changes.

In the case of thick snow cover at a warmer air temperature of -10°C, the thermodynamic model produces a smaller temperature gradient within the snow/ice system. Compared to the cold and warm cases of thin snow in Figure 3, the cases for thick snow in Figure 5 show a smaller increase in surface temperatures commanding a smaller increase in brine volumes. Since the thermodynamically driven brine distribution is important to the backscatter, as indicated in the above results, the backscatter change due to the thermal effects will be related to the snow thickness.

We couple the thermodynamic changes induced by the thick snow cover with the microwave model to estimate the consequent effects on the backscatter change. The average parameters are presented in Tables 4 and 5 for the thick cold snow and thick warm snow cases, respectively. We use the thermally modified values for brine volumes, brine geometry, and permittivities in the 8-cm basal snow layer and 1.7-m FY ice layer to calculate the backscatter for the cold and warm cases. The same roughness for smooth FY ice is also applied to these cases. The model results are listed in Table 6 for effective permittivities and backscatter. The results show: 1) an increase in backscatter from -22.1 dB to -19.7 dB between thin cold snow and thick cold snow cases, 2) a slight change in backscatter from -18.6 dB to -19.0 dB for thin warm snow and thick warm snow cases, and 3) consequently a smaller increase of 0.7 dB in the backscatter for the thick warm and cold cases compared to the backscatter increase of 3.5 dB for the thin snow cover cases. Note that the temperature dependence of wave propagation and associated changes in scattering loss in the layered system are accounted for with the temperature dependent effective permittvities.

These modelling results indicate that we can expect a larger change in scattering, between a warm and cold condition surface, for a thin snow cover relative to a thick snow cover. This change will only be detectable if the following conditions are met: 1) sufficient amount of brine in the basal layer of the snow and within the surface frazil layer of the first-year sea ice, 2) a surface geometry which can be considered 'smooth' within the Kirchoff limits used here, and 3) kinetic growth snow grains and brine inclusions of

sufficient sizes within the basal snow layer and the surface frazil ice layer to become scattering centres at 5.3 GHz.

4.3. Observational Evidence

Comparison of two different ERS-1 subscenes shows that there is a detectable increase in scattering between cold and warm atmospheric temperatures (Figure 6). The bivariate histogram shows a significant increase in scattering for targets below about -19 dB. Our working hypothesis throughout this paper is that the thickness of the snow cover should determine how much the scattering changes between the cold and warm cases. Our premise is that a thicker snow cover will result in less thermodynamically related change at the snow/ice interface and this will translate into a smaller change in scattering.

To further examine the ERS-1 data we first separated the scene into those pixels with a scattering magnitude of less than -19 dB, since this is our primary range of interest. We then geometrically corrected the May 9 scene to the May 6 scene and constructructed a change detection image by subtracting the two dates (Figure 7A). This change map illustrates the magnitude of the change in scattering over smooth first-year sea ice targets. Given the coherent fading statistics of radar, and errors in the geometric correction we can expect a relatively 'noisy' change image. To examine the trend in the scattering change we present two common filtering techniques: a 5x5 median filter (B) and a 5x5 Gaussian filter (C). Visually, both of these filtered images suggest a pattern to the change in magnitude between May 6 and May 9. By combining a contour plot of the average change trend surface we can produce a visually informative map of both the location and magnitude of the change in scattering (Figure 7 D).

Qualitatively, it would appear that the change in SAR scattering over smooth first-year sea ice follows a pattern which closely resembles the general ice and snow thickness conditions as defined by the consolidation periods (as presented in Figure 1). We can see that in the earliest consolidation period (point 1 in Figure 8) there is only a slight change in scattering and that the largest contours of change are located fairly close to land. In the second consolidation area the snow thickness is somewhat lower (Figure 1) and the change in scattering appears to increase (point 2 in

Figure 8). The largest change in scattering is observed south and East of Griffith Island. This area corresponds very closely to the January consolidation area which had between 10 and 15 cm of snow (about 50 percent of that in the September consolidation area). Point 4 (Figure 8) appears to have an observable amount of change in scattering. We are unsure of the ice and snow thickness conditions in this area because we did not visit it during the field program.

Point 5 appears to be a location of little or no change in scattering. This area consolidated very late in March and was only 30 cm thick by the time of our field program. We modelled the snow/ice interface temperature [4] under a range of snow thickness conditions for a thick (1.85 m) and thin (0.3 m) sea ice (Figure 9). For an increase in the air temperature from -20 to -10°C with a 10-cm snow cover, the results show that the snow/ice interface temperature increase from -8 to -5°C for the thin ice case, compared to a larger change from -16 to -8°C for the 1.8 m thick ice case. However, the slope of the phase eutectic curve is steeper over the range of temperature in the thin ice case, and the overall redistribution of brine volume distribution is effectively similar for both cases. Thus, the lack of backscatter change over point 5 may be caused by other effects such as rough surface scattering, which is less sensitive to the interface temperature. Also note the dark spot appears in Figures 7 and 8 on the right side of the January consolidation area, which corresponds to a multi-year ice floe containing too little surface salinity to effectuate the thermal effect on backscatter.

It is interesting to note that when we initialized our forward scattering model with the average geophysical conditions measured in situ, that we observe strong agreement for both the magnitude and change in scattering between the model and the ERS-1 data (Figure 9). Both the geophysical conditions and their thermodynamic relationships appear to be well represented in the scattering model. This lends considerable support to the notion of developing invertable models of the sea ice scattering conditions which may be used for the inversion of both geophysical and thermodynamic characteristics of snow covered smooth first-year sea ice.

5. Conclusions

Both our modelling and observational evidences suggest that the average relative scattering coefficient at 5.3 GHz (VV pol) is sensitive to the thermodynamic structure of the snow/sea ice system. It appears that changes to the snow/sea ice thermodynamics are detectable in time series SAR data. We conclude that within the conditions of this case study there is a detectable change in scattering over low-magnitude ice types such as smooth first-year sea ice. Changes are not detectable over multiyear or rough forms of first-year sea. The change in scattering between air temperatures of -18 and -11°C resulted in a increase in the snow/ice interface temperature. This change caused an increase in the complex permittivity of the snow basal layer and within the surface frazil layer of the sea ice. The change in scattering is well within the detection capabilities of most spaceborne SAR (1-3 dB). The physical mechanisms causing the change are, in order of relevance: the brine pockets within this basal layer, the brine pockets within the frazil layer, and the ice surface roughness.

An increase in air temperature is shown to increase scattering over smooth first-year sea ice. The increase in scattering appears to be related, at least in the first order, to the thickness of the snow cover over first-year sea ice. For a given ice thickness and air temperature change, a thick snow cover will result in a smaller change in the snow/ice interface temperature (due to the thermal conductivity of the snow cover). This small change in the interface temperature will result in a relatively small change in the brine volume at the interface and the resulting complex permittivity, thereby producing a relatively small change in scattering. A thin snow cover produces a larger interface temperature change and thereby a larger change in scattering. It is important to note that the microwave scattering change is responding to the brine volume and complex permittivity of the snow/ice interface and that this interface will be dominated by thermodynamic forcing in the OSA system.

The results presented here represent a significant evolution in our understanding of how we can use microwave remote sensing for studies of ocean-sea ice-atmosphere processes. Our results suggest that we can now look to using SAR as a means of determining not only the geophysical state of the snow/sea ice system but, given certain caveats, we can also assess the

thermodynamic state of the system. The first practical application of this theory may be in the estimation of snow thickness classes over sea ice. We are currently conducting a dedicated validation of the theory presented here to determine the range of conditions over which this theory is valid. Other thermodynamically related issues such as the strength of sea ice, ablation state and estimation of ice thickness are also being investigated [*Barber et al.*, 1998; *Yackel and Barber*, 1997].

Acknowledgements

The research by the University of Manitoba (DGB) is supported by the Canadian Ice Services, the Natural Sciences and Engineering Research Council of Canada, and grant N00014-94-1-03-86 from the Office of Naval Research. The research performed by the Center for Space Microelectronics Technology, Jet Propulsion Laboratory, California Institute of Technology (SVN), was sponsored by the Office of Naval Research (ONR) through an agreement with the National Aeronautics and Space Administration. Thanks to M. Shokr for the sea ice microstructure data, the Polar Continental Shelf Project for logistical support, and to the participants in the SIMMS'93 experiment.

References

Barber, D. G., *Assessment of the Interaction of Solar Radiation (0.3 to 3.0 μm) with a Seasonally Dynamic Snow Covered Sea Ice Volume, from Microwave (2.0 to 5.0 cm) Scattering. PhD Dissertation.* Earth Observations Lab., Department of Geography, University of Waterloo, Ontario, Canada, 266 pp., 1992.

Barber, D. G., S. P. Reddan, and E. F. LeDrew, Statistical characterization of the geophysical and electrical properties of snow on landfast first-year sea ice, *J. Geophys. Res.*, *100*(C2), 2673-2686, 1994a.

Barber, D. G., T. N. Papakyriakou, and E. F. LeDrew, On the relationship between energy fluxes, dielectric properties, and microwave scattering over snow covered first-year sea ice during the spring transition period, *J. Geophys. Res.*, *99*(C11), 22401-22411, 1994b.

Barber, D. G., T. N. Papakyriakou, E. F, LeDrew. and S. Shokr, An examination of the relationship between the spring period evolution of the scattering coefficient (σ°) and energy fluxes over landfast sea ice, *Int. J. Remote Sens.*, *16*(17), 3343-3363, 1996.

Barber, D. G., and A. Thomas, The influence of cloud cover on the radiation budget, physical properties and microwave scattering coefficient of first-year and multi-year sea ice, *IEEE Trans. Geosci. Remote Sens.*, in press, 1998.

Barber, D. G., J. Yackel, R. Wolfe, and W. Lumsden, Estimating the thermodynamic state of snow covered sea ice using time series synthetic aperture radar (SAR) data, *Int. Soc. Offshore Petrol. Eng.*, in review. 1998.

Barry, R. G., M. C. Serreze, and J. A. Maslanik, The Arctic sea ice-climate system: Observations and modeling, *Rev. Geophys.*, *31*(4), 397-422, 1993.

Clausi, D., and T. Zagon, *Microscale Surface Roughness Measurements of Sea Ice*, Sec. 6.7, in K. Misurak, D. G., Barber, and E. F. LeDrew, SIMMS'93 data report, Earth Obs. Lab. Tech. Rep., ISTS-EOL-SIMS-TR-93-007, 1993.

Colbeck, S. C., An overview of seasonal snow metamorphism, *Rev. Geophys. Space Phys.*, *20*(1), 45-61, 1982.

Colbeck, S. C., Classification of seasonal snow cover crystals, *Water Resources Res.*, *22*(9), 59-70, 1986.

Cota, G. F., and E. P. W. Horne, Physical control of Arctic ice algal production, *Marine Ecol. Prog. Ser.*, *52*, 111-121, 1989.

Cox, G. F. N., and W. F. Weeks, Equations for determining the gas and brine volumes in sea-ice samples, *J. Glaciol.*, *29*(12), 306-316, 1983.

Cox, G. F. N., and W. F. Weeks, Numerical simluations of the profile properties of undeformed first year sea ice during the growth season, *J. Geophys. Res.*, *93*(C10), 12449-12460, 1988.

Grenfell, T. G., and G. A. Maykut, The optical properties of ice and snow in the Arctic basin., *J. Glaciol.*, *18*(80):445-463, 1977.

Klein, L. A., and C. Swift, An improved model for the dielectric constant of sea water at microwave frequencies, *IEEE Trans. Antennas Propagat.*, *AP-25*(1), 104-111, 1977.

LeDrew, E. F., and D. G. Barber, The SIMMS program: A study of change and variability within the marine cryosphere, *Arctic*, *47*(3), 256-264, 1994.

Maykut, G. A., Energy exchange over young sea ice in the central Arctic, *J. Geophys. Res.*, *83*(C7), 3646-3658, 1978.

Nakawo, M., and N. K. Sinha, Growth rate and salinity profile of first-year sea ice in the High Arctic, *J. Glaciol.*, *27*(96), 315-330, 1981.

Nghiem, S. V., R. Kwok, J. A. Kong, and R. T. Shin, A model with ellipsoidal scatterers for polarimetric remote sensing of anisotropic layered media, *Radio Sci.*, *28*(5), 687-703, 1993.

Nghiem, S. V., R. Kwok, S. H. Yueh, J. A. Kong, C. C. Hsu, M. A. Tassoudji, and R. T. Shin, Polarimetric scattering from layered media with multiple species of scatterers, *Radio Sci.*, *30*(4), 835-852, 199a.

Nghiem, S. V., R. Kwok, S. H. Yueh, and M. R. Drinkwater, Polarimetric signatures of sea ice, 1, Theoretical model, *J. Geophys. Res.*, *100*(C7), 13665-13679, 1995b.

Nghiem, S. V., R. Kwok, J. A. Kong, R. T. Shin, S. A. Arcone, and A. J. Gow, An electrothermodynamic model with distributed properties for effective permittivities of sea ice, *Radio Sci.*, *31*(2), 297-311, 1996.

Nghiem, S. V., R. Kwok, S. H. Yueh, D. K. Perovich, A. J. Gow, C. C. Hsu, K. H. Ding, J. A. Kong, and T. C. Grenfell, Diurnal thermal cycling effects on backscatter of thin sea ice, *IEEE Trans. Geosci. Remote Sens.*, in press, 1997.

Olmsted, *Alaska SAR facility scientific SAR user's guide*, ASF-SD-003, Alaska SAR Facility Tech. Rep., Geophysical Institute, U. of Alaska, Fairbanks, 1993.

Shokr, M. E., personal communication (Field observation of brine pocket size in frazil sea ice), 1997.

Shokr, M. E., and N. K. Sinha, Arctic sea ice microstructure observations relevant to microwave scattering, *Arctic*, *47*(3), 265-279, 1994.

Smith, T. G., and I. Stirling, Variation in the density of ringed seal (Phoca hispida) birth lairs in the Amundsen Gulf, Northwest Territories., *Can. J. Zoology*, *56*, 1066-1070, 1977.

Stogryn, A., and G. J. Desargant, The dielectric properties of brine in sea ice at microwave frequencies, *IEEE Trans. on Antennas and Propagat.*, *AP-33*(5), 523-532, 1985.

Tiuri, M. E., A. H. Sihvola, E. G. Nyfors, and M. T. Hallikainen, The complex dielectric constant of snow at microwave frequencies, *IEEE J. Ocean Eng.*, *OE-9*(5), 377-382, 1984.

Tsang, L., and J. A. Kong, Scattering of electromagnetic waves from random media with strong permittivity fluctuations, *Radio Sci.*, *16*(3), 303-320, 1981.

Vant, M. R., R. O. Ramseier, and V. Markios, The complex dielectric constant of sea ice at frequencies in the range 0.1-40 GHz, *J. Appl. Phys.*, *49*(3), 1264-1280, 1978 (also see erratum by Vant et al., *J. Appl. Phys.*, *53*(2), 1269, 1982).

Welch, H.E. and M.A. Bergmann. Seasonal development of ice algae and its prediction from environmental factors near Resolute, N.W.T., Canada, *Can. J. Fisher. Aquatic Sci.*, *46*, 1793-1804, 1989.

Yackel., J., and D. G. Barber, On the links between theromdynamic, electrical, mechanical and microwave scattering over snow covered landfast first-year sea ice, *Can. J. Remote Sens.*, in review, 1997.

Yueh, H. A., R. T. Shin, and J. A. Kong, Scattering from randomly oriented scatterers with strong permittivity fluctuations, *J. Electromag. Wave Theory Applic.*, *4*(10), 983-1004, 1990.

List of Figures

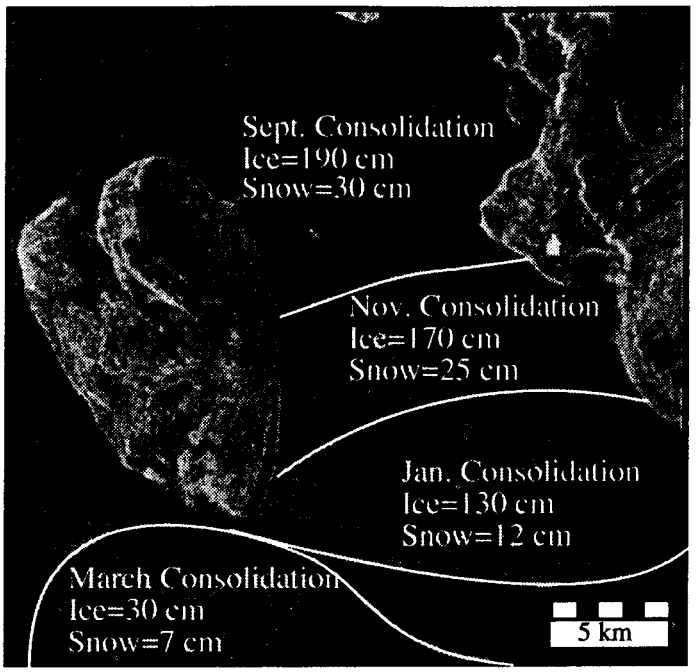

Figure 1. Seasonal Sea Ice Monitoring and Modelling Site (SIMMS) field location for the period April - July, 1993. Consolidation periods and average snow and ice thickness conditions are denoted within 4 different consolidation zones within the study area.

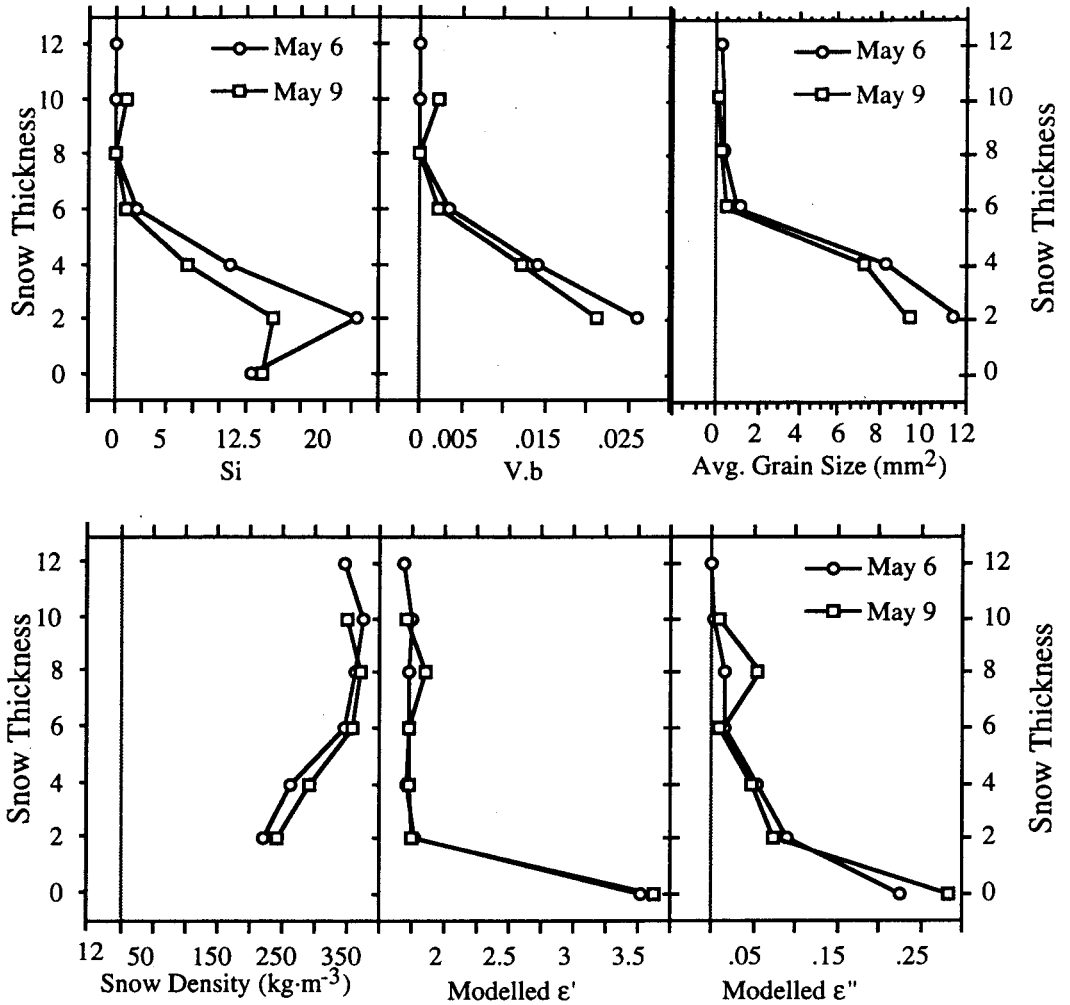

Figure. 2. Profile plots of first-year (FY1) snow and ice surface salinity (Si), brine volume (V.b), temperature of the snow volume (T°snow) and ice volume (T°ice), average grain area, snow density, modelled dielectric permittivity (ε') and loss (ε'''). All variables were measured in situ at approximately solar noon on May 6 and May 9, 1993.

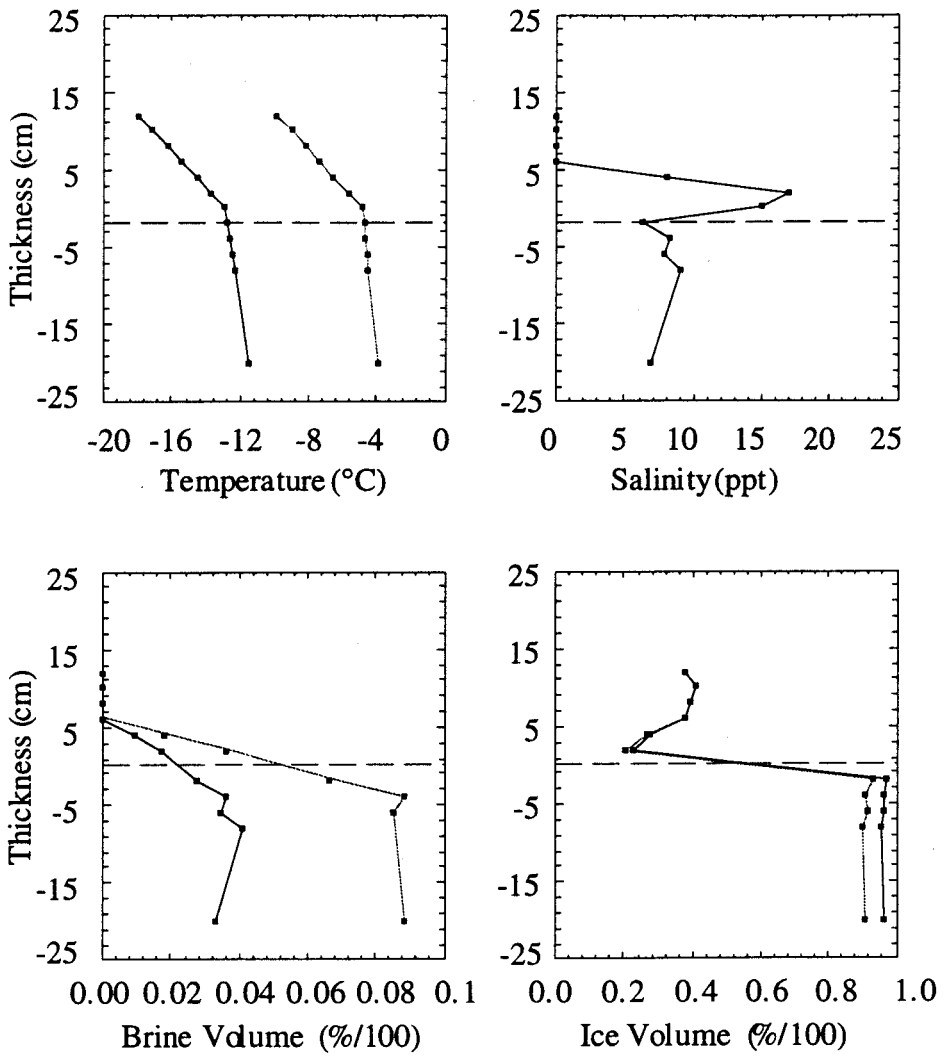

Figure 3. Thin snow case physical parameters for the cold and warm conditions used to initialize the forward scattering model.

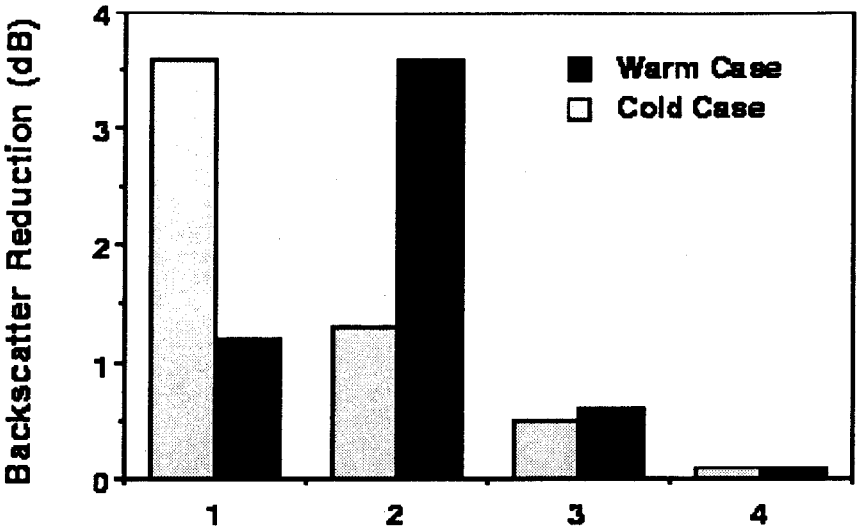

Figure 4. Reduction in backscatter from full scattering mechanisms by: 1) eliminating scattering from ice grains in snows, 2) eliminating scattering from brine inclusions in snow, 3) eliminating scattering from brine pockets in frazil ice, and 4) eliminating rough surface at the interface between snow and sea ice.

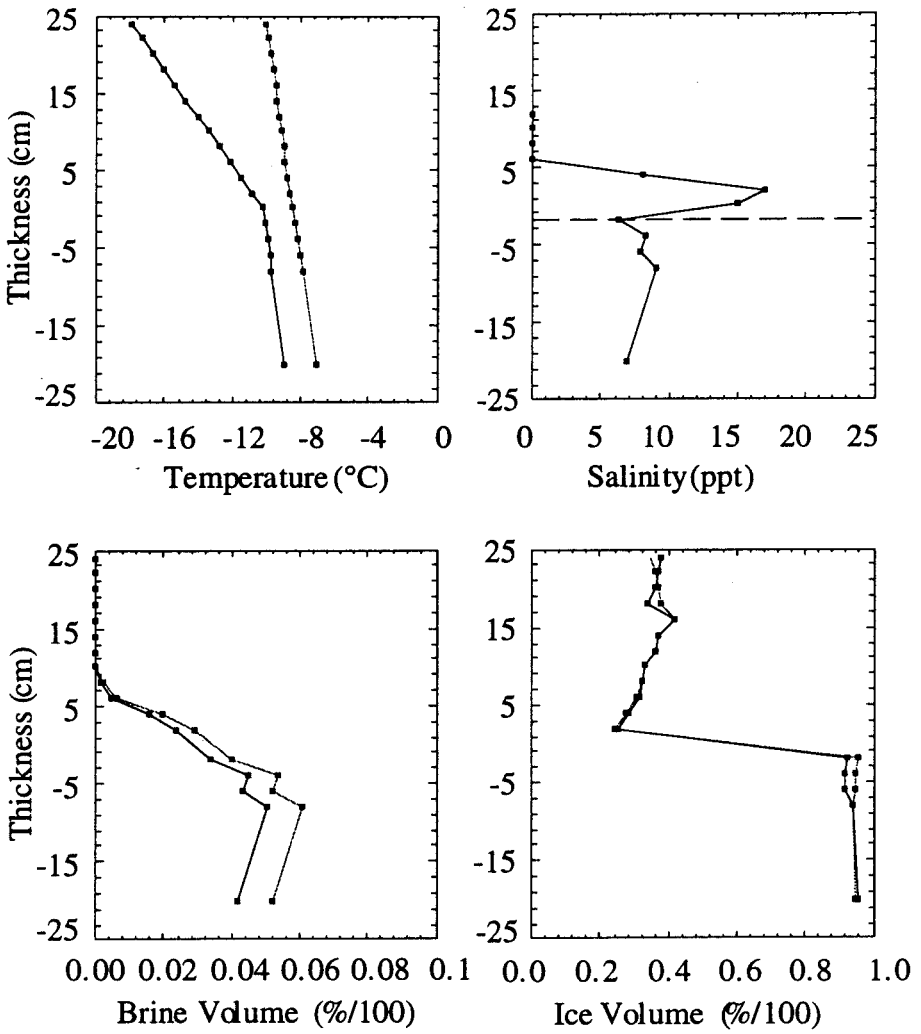

Figure 5. Thick snow case physical parameters for the cold and warm conditions

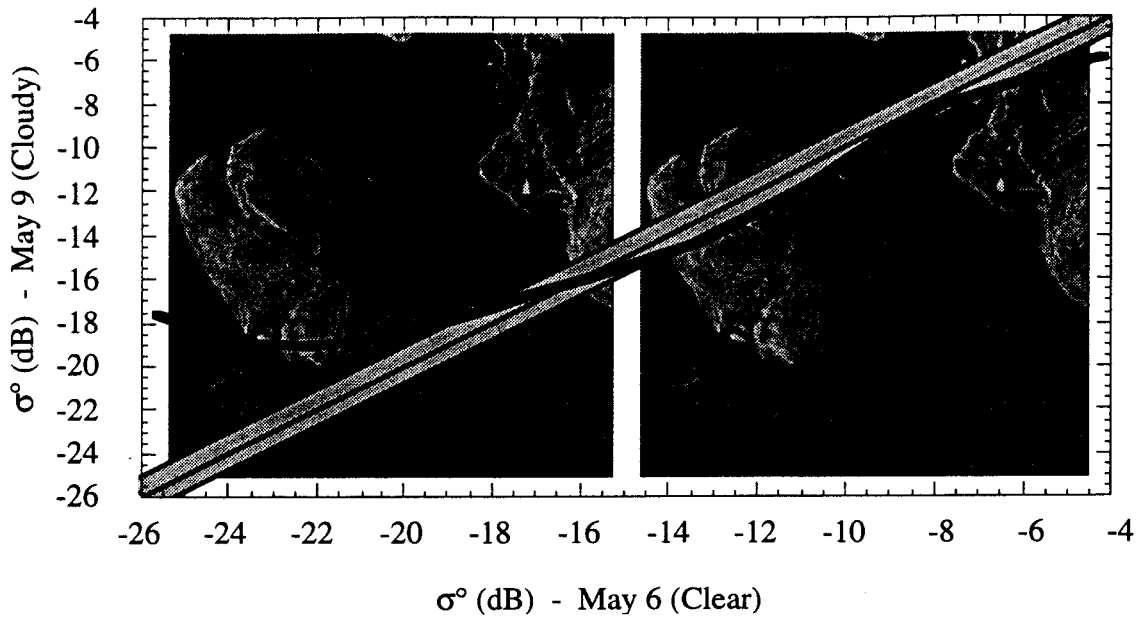

Figure 6. Bivariate plots of cold and warm cases from ERS-1 backscatter.

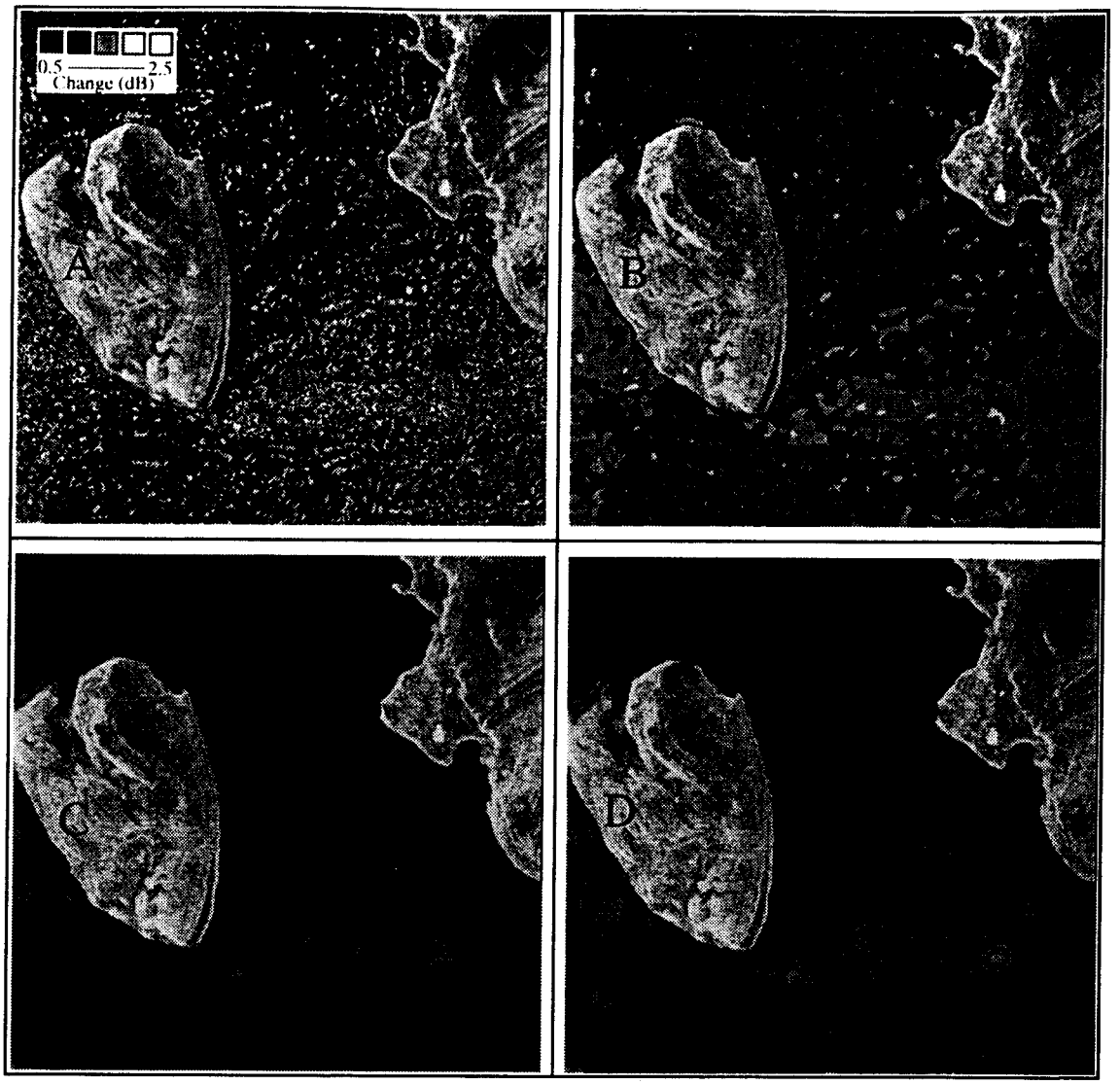

Figure 7. ERS-1 data showing the spatial relationship between the May 6 and May 9 scattering conditions. Change detection is computed by subtracting the 2 dates (A). This change image is then filtered using a 5x5 median convolution kernal (B) and a 5x5 Gaussian filter. The trend in the scattering change is them contoured to illustrate the location and magnitude in the change in scattering (D).

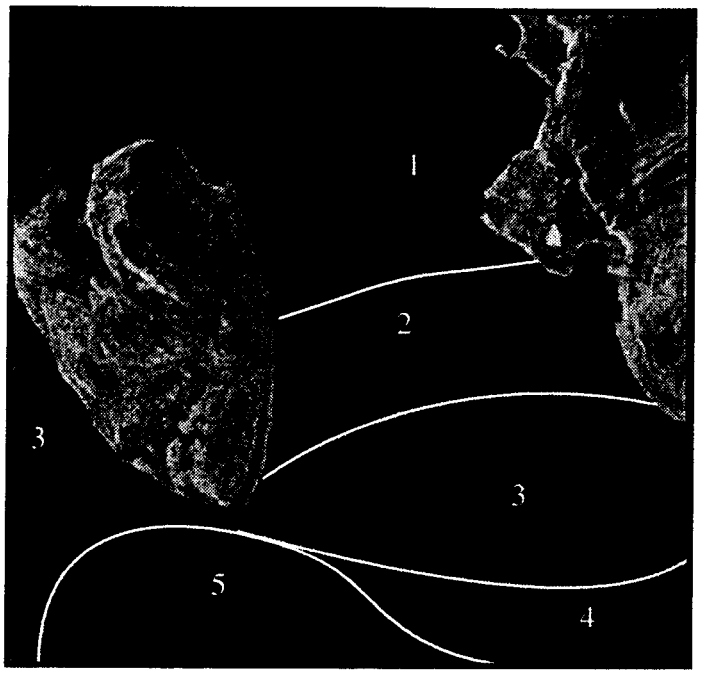

Figure 8. General relationship between consolidation conditions and the trend surface for change in scattering between May 6 and May 9.

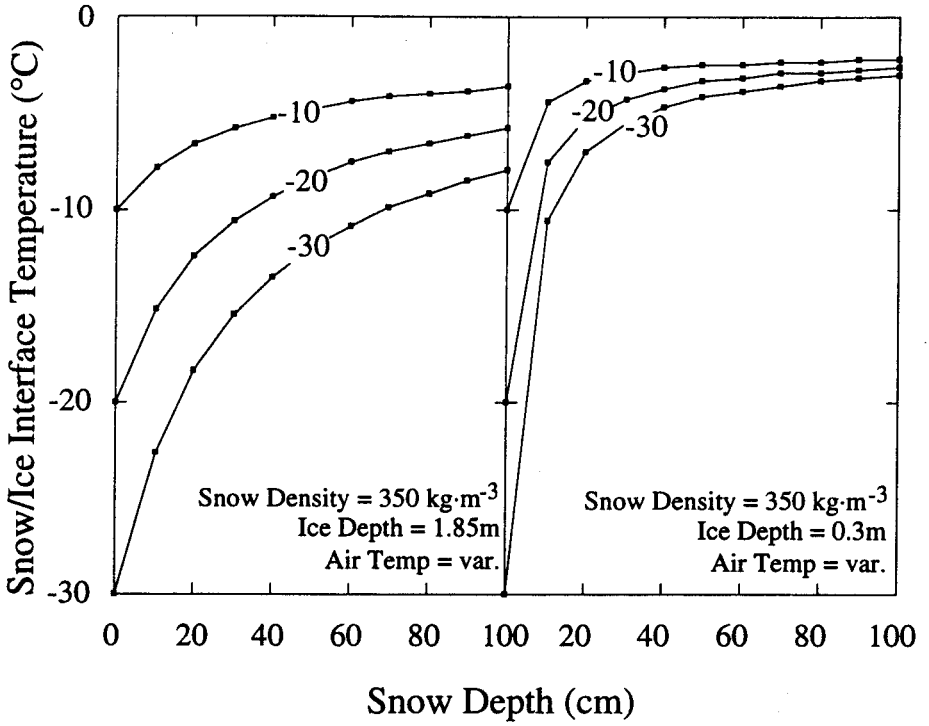

Figure 9. Modelled relationship between ice thickness, snow thickness, air temperature and the snow/ice interface temperature. The curves depict air temperatures of -10, -20 and -30°C. The change in the snow/ice interface temperature is larger when the ice cover is thick.

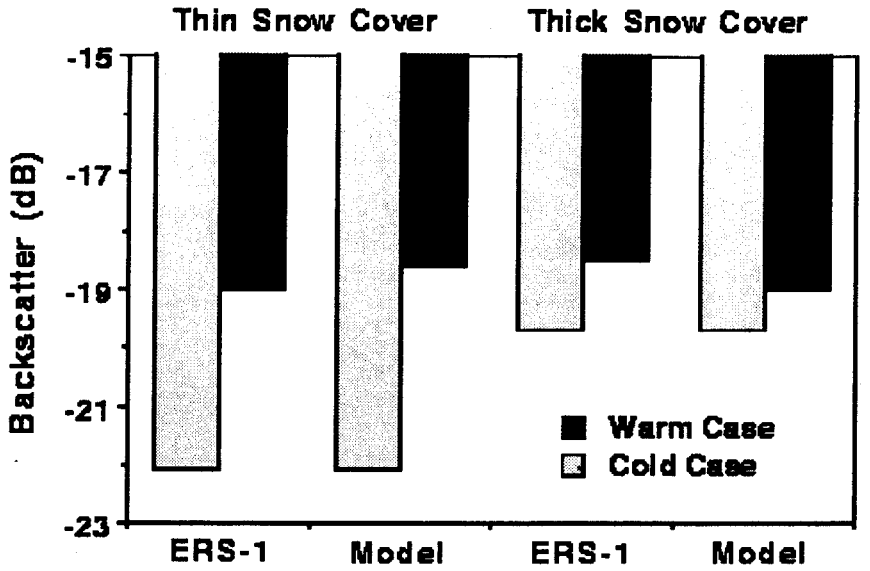

Figure 10. Modelled and ERS-1 scattering results for the thin and thick snow cover cases showing a good agreement both in magnitude and change in scattering over the range of conditions examined here.